Energy and heat fluxes due to vertically propagating Yanai waves observed in the equatorial Indian Ocean

Citation	Smyth, W. D., Durland, T. S., & Moum, J. N. (2015). Energy and heat fluxes due to vertically propagating Yanai waves observed in the equatorial Indian Ocean. Journal of Geophysical Research: Oceans, 120(1), 1-15. doi:10.1002/2014JC010152
DOI	10.1002/2014JC010152
Publisher	American Geophysical Union
Version	Version of Record
Terms of Use	http://cdss.library.oregonstate.edu/sa-termsofuse

AGU PUBLICATIONS

JGR

Journal of Geophysical Research: Oceans

RESEARCH ARTICLE

10.1002/2014JC010152

Energy and heat fluxes due to vertically propagating Yanai waves observed in the equatorial Indian Ocean

W. D. Smyth[1], T. S. Durland[1], and J. N. Moum[1]

[1]College of Earth, Ocean and Atmospheric Sciences, Oregon State University, Corvallis, Oregon, USA

Key Points:
- Oscillations in the equatorial Indian Ocean were identified as Yanai waves
- The energy flux is similar to midlatitude near-inertial waves
- Meridional heat flux is comparable to model results

Correspondence to:
W. D. Smyth,
smyth@coas.oregonstate.edu

Citation:
Smyth, W. D., T. S. Durland, and J. N. Moum (2015), Energy and heat fluxes due to vertically propagating Yanai waves observed in the equatorial Indian Ocean, *J. Geophys. Res. Oceans*, *120*, 1–15, doi:10.1002/2014JC010152.

Received 22 MAY 2014
Accepted 8 DEC 2014
Accepted article online 16 DEC 2014
Published online 9 JAN 2015

Abstract Shipboard current measurements in the equatorial Indian Ocean in October and November of 2011 revealed oscillations in the meridional velocity with amplitude $\sim 0.10\,\mathrm{m/s}$. These were clearest in a layer extending from ~300 to 600 m depth and had periods near 3 weeks. Phase propagation was upward. Measurements from two sequential time series at the equator, four meridional transects and one zonal transect are used to identify the oscillation as a Yanai wave packet and to establish its dominant frequency and vertical wavelength. The Doppler shift is accounted for, so that measured wave properties are translated into the reference frame of the mean zonal flow. We take advantage of the fact that, in the depth range where the wave signal was clearest, the time-averaged current and buoyancy frequency were nearly uniform with depth, allowing application of the classical theoretical representation of vertically propagating plane waves. Using the theory, we estimate wave properties that are not directly measured, such as the group velocity and the zonal wavelength and phase speed. The theory predicts a vertical energy flux that is comparable to that carried by midlatitude near-inertial waves. We also quantify the wave-driven meridional heat flux and the Stokes drift.

1. Introduction

Yanai waves are a prominent mode of variability in the equatorial atmosphere and oceans [*Wheeler and Kiladis*, 1999; *Shinoda*, 2012; *Chatterjee et al*., 2013]. Here we describe shipboard observations on the equator at 80.5E longitude, in the central Indian Ocean, which revealed a packet of oceanic Yanai waves propagating downward through a layer of relatively uniform currents and stratification. This uniformity allows detailed comparison with the classical dispersion relation for vertically propagating equatorial waves and the inference of wave parameters not measurable directly. The shipboard measurements are valuable because the uniform layer is beyond the range of the current profiler on the nearby RAMA mooring (Research Moored Array for African-Asian-Australian Monsoon Analysis and Prediction) [*McPhaden et al*., 2009]. The waves appear to have been generated to the west of our location during the previous monsoon season.

Yanai waves, also called mixed Rossby-gravity waves, were predicted in the early theoretical work of *Matsuno* [1966] and observed soon after this [*Yanai and Murayama*, 1966]. Their importance in the atmosphere is well established; they carry momentum high into the stratosphere where it is dissipated, thereby driving the stratospheric quasi-biennial oscillation [*Holton and Lindzen*, 1972]. The oceanic manifestation was first observed in the eastern Atlantic by *Weisberg et al*. [1979] and has since been studied extensively in the Pacific [e.g., *Farrar and Durland*, 2012]. Indian Ocean observations of Yanai waves were made initially in the west, where they were first evident in the analyses of *Luyten and Roemmich* [1982] and *O'Neill* [1984]. In this region, observations and models have shown that Yanai waves are generated locally by meridional winds, most strongly during the southwest monsoon, as well as by dynamic instabilities and by reflections of Rossby waves from the Somali coast [e.g., *Kindle and Thompson*, 1989; *Moore and McCreary*, 1990; *Kelly et al*., 1995; *Chatterjee et al*., 2013].

Because their group velocity is always eastward, Yanai waves generated in the western Indian Ocean are likely to propagate to the central and eastern regions [e.g., *Miyama et al*., 2006]. *Sengupta et al*. [2004] and *Masumoto et al*. [2005] observed a distinct band of waves with periods in the 10–20 day range. Using an ocean model, *Sengupta et al*. [2001] and *Sengupta et al*. [2004] identified the oscillations as Yanai waves forced locally by fluctuating meridional winds. Yanai waves were found to intensify toward the east (the direction of energy propagation) due to an accumulation of energy by local forcing and to the absence of waves reflected from the eastern coast in this frequency band.

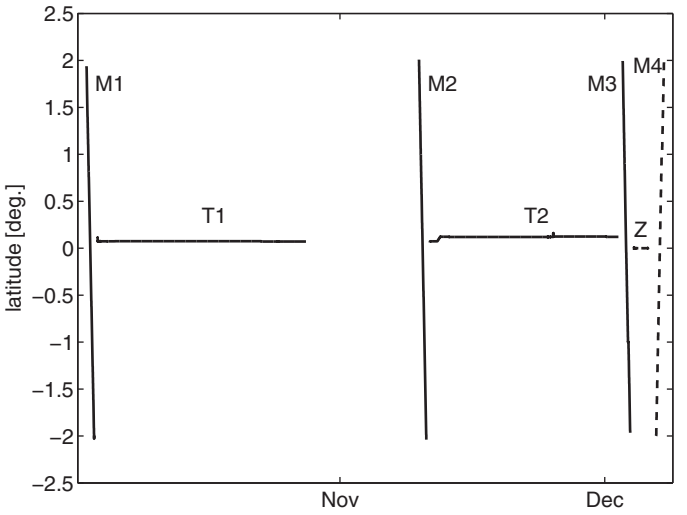

Figure 1. Track of the R/V Revelle during legs 2 and 3 of DYNAMO, 3 October to 7 December 2011. Labels indicate time series (T1,T2), meridional transects (M1–M4) and a zonal transect (Z). Longitude is 80.5E except for Z and M4 (dotted curves; see Table 1 for details).

Yanai waves are capable of generating steady zonal currents that extend to great depths [e.g., *d'Orgeville et al*., 2007], possibly explaining deep jets observed in the Indian Ocean [*Dengler and Quadfasel*, 2002]. *Ogata et al*. [2008] noted the possibility for biweekly Yanai wave energy to propagate vertically into the deep ocean [also see *Miyama et al*., 2006; *Ascani et al*., 2010]. The energy flux due to vertically propagating Yanai waves has been measured in the Pacific [*Eriksen*, 1982] but not, to our knowledge, in the Indian Ocean where monsoon forcing could lead to a very different wave regime. Here we describe observations of that propagation and assess the associated vertical energy flux in comparison to Yanai wave fluxes in the equatorial Pacific [*Eriksen*, 1982] and to near-inertial waves at higher latitudes [e.g., *Alford*, 2003; *Cuypers et al*., 2013].

Heat fluxes due to Yanai waves have been explored recently by *Nagura et al*. [2014] in observations and model simulations. Here we extend that work by showing that equatorial flux convergence occurs as a consequence of downward energy propagation and give a simple formula (valid for all even modes) to estimate its magnitude based on measurable wave properties. We also compare with fluxes due to tropical instability waves in the Pacific [*Hansen and Paul*, 1984] and discuss uncertainties in the actual heating that might accompany this flux convergence.

We begin in section 2 with a description of the measurements used in this study. In section 3, we give an overview of wavelike features in the meridional velocity record and the environment through which they propagated. In section 4, we show that the observations can be understood in terms of the linear theory for plane Yanai waves in a uniformly stratified environment. The main results are in section 5. There, we combine the theory with the observations to obtain estimates for various wave parameters that we cannot measure directly and compare the results with previous studies of Yanai waves. We begin with parameters describing the basic spatial and temporal scales (section 5.1). We then evaluate vertical energy flux (section 5.2) the convergence of the meridional heat flux (section 5.3) and the Stokes drift velocity (section 5.4). Conclusions are summarized in section 6.

2. Observations

In Fall 2011, as part of the DYNAMO field program aimed at studying the onset of the Madden-Julian Oscillation (MJO), the R/V Revelle undertook a 9 week measurement program in the central Indian Ocean [*Moum et al*., 2014]. The cruise spanned 65 days, with a 14 day interruption for reprovisioning (Figure 1 and Table 1). The first segment (DYNAMO leg 2) began with a meridional transect along 80.5E from 2N to 2S (labeled M1 in Figure 1). The ship then remained on station at 0N, 80.5E for 23.6 days (T1). After reprovisioning, we executed a second, identical meridional section (M2), then remained at 0N 80.5E for 21.4 days. We then conducted a third section from 2N to 2S at 80.5E (M3), a zonal section along the equator from 80.5E to 90E (Z), and a fourth meridional section (M4) from 2S to 2N at 90E (Figure 1).

Table 1. Periods, Longitudes, and Latitudes of the Transects Shown on Figure 1[a]

	Start	End	Longitude	Latitude
M1	10/3 06:43	10/4 03:36	80.5E	2N–2S
T1	10/4 12:58	10/28 03:36	80.5E	0
M2	11/9 22:48	11/10 18:50	80.5E	2N–2S
T2	11/11 04:33	12/2 13:12	80.5E	0
M3	12/3 00:43	12/3 21:07	80.5E	2N–2S
Z	12/4 07:41	12/6 08:10	80.5E–90E	0
M4	12/6 19:41	12/7 17:02	90E	2S–2N

[a]Time format is "month/day hour:minute," UTC, in 2011. Longitude and latitude are in degrees.

Meteorological measurements, air-sea fluxes and upper ocean currents, hydrography and

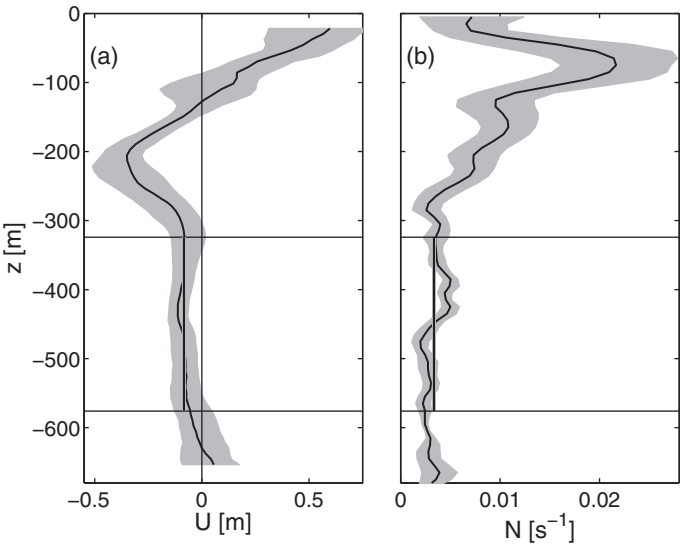

Figure 2. (a) Mean zonal velocity and (b) mean buoyancy frequency at 0N 80.5E. The range is one standard deviation. Horizontal lines indicate the depth range $-576 < z < -324$m referred to in subsequent analyses as the wave layer. Vertical lines show mean values in the wave layer.

microstructure were all sampled. A regime of interest for DYNAMO was the eastward flowing Wyrtki Jet and its westward flowing undercurrent, which occupied approximately the upper 300 m of the ocean. In this paper, however, our focus is the layer beneath these surface currents, extending from 300 to 600 m depth. An RDI broadband acoustic Doppler current profiler (ADCP) was operated at 75 kHz and provided useful data in 16 m bins extending to 600 m and deeper. For the present analysis, this data was combined with 87 casts with a Seabird conductivity-temperature-depth (CTD) profiler, which extended from the surface to 200–1000 m and were located within 0.2° of 0N 80.5E.

3. Overview of Currents and Stratification

The time average of the observed zonal current U (Figure 2a) was dominated by the eastward Wyrtki jet which extended, on average, to 140 m depth, and the westward equatorial undercurrent which extended from the base of the Wyrtki jet to about 300 m. Below this was a layer of relatively uniform westward flow extending nearly to 600 m.

The time-averaged buoyancy frequency N was a maximum in the seasonal pycnocline between 50 and 100 m depth. Below this, N decreased down to about 300 m, then remained within a factor of two of 3.37×10^{-3}s^{-1} down to about 1000 m. The uniformity of both the mean current and the stratification in this layer is exploited in the analyses to follow.

Below the equatorial undercurrent, the time-dependent zonal velocity field u (Figure 3a) showed a weak westward mean flow modulated by a disturbance with upward-propagating isotachs whose period was evidently longer than our data record. This may represent the westward phase of a long-period Kelvin or Rossby wave. If so, our data record covers at most one half-period, and the period is therefore at least 110 days. This is consistent with the 182 day periodicity of the Wyrtki jet and its associated undercurrent [*Wyrtki*, 1973; *Luyten and Roemmich*, 1982; *Nagura and McPhaden*, 2008, 2010].

The meridional velocity v (Figure 3b) fluctuated rapidly near the surface. Near 100 m depth, thin currents fluctuated on a longer time scale, reversing sign once in the course of our observations. Below 300 m, the meridional velocity shows an oscillation with upward-propagating isotachs. Its period was much shorter than that of the zonal oscillation in the same depth range (cf. Figure 3a). This independence of the zonal and meridional oscillations suggests that they resulted from distinct equatorial wave modes.

At least one complete period of the meridional oscillation is captured in our data record, and that oscillation is therefore our focus in this paper. Sloping lines on Figure 3b highlight coherent minima and maxima that suggest crests and troughs. The upward phase propagation suggests an equatorial wave packet with downward energy propagation [e.g., *McCreary*, 1984]. The wave signal is most clearly defined in the meridional velocity record from the time series T2 (11 November to 2 December), showing a northward and a southward phase followed by what may have been the beginning of a new northward phase below 400 m depth in the last few days of the station. Measurements from T1 show a southward current that was likely part of the same wave, though the data gap makes it hard to be certain. Prior to this was a period of mainly

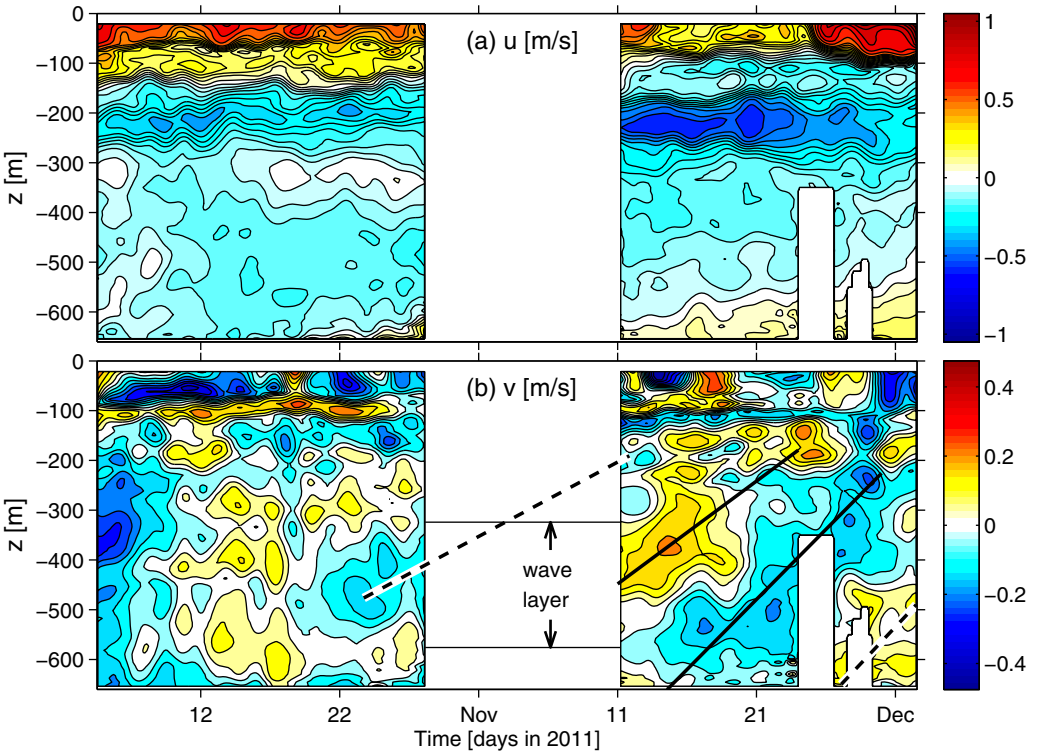

Figure 3. (a) Zonal and (b) meridional velocity components measured by ADCP during two legs of DYNAMO. Time dependence is lowpass filtered with a 2 day minimum period to remove tides. White bands indicate missing or unreliable data. Sloping lines in Figure 3b highlight possible upward phase propagation in the meridional velocity. Solid lines show a crest and a trough that were relatively well captured in the measurements; dashed lines indicate another crest and trough whose existence is more speculative.

northward flow (12–22 October) that we interpret as the first indication of the wave packet's arrival. The wave signal is not evident in transects Z and M4, suggesting that the trailing edge of the wave packet passed 0N, 80.5E during the first few days of December.

4. Identification of the Meridional Oscillation as a Yanai Wave Packet

In this section, we will demonstrate that the observed oscillations in meridional velocity (Figure 3b) are consistent with a vertically propagating Yanai wave packet [e.g., *Matsuno*, 1966; *Moore and Philander*, 1977; *Gill*, 1982; *McCreary*, 1984] (see summary in Appendix A). To do this, we estimate the dominant frequency and vertical wave number during the time when the signal was strongest, and compare it with the dispersion relation for linear, vertically propagating, equatorially trapped plane waves to identify the wave type. With this information, we can then use the theory to infer other wave properties that were not directly observed.

Linear, vertically propagating plane waves exist only in a vertically infinite domain. To interpret observations made in the finite ocean in terms of this idealization, we assume that boundary effects were not important at our location. This assumption is justified because the inferred plane wave is evidently the dominant component of a wave packet which, besides dissipating, would reflect to a different location and would not return to the depth range of interest until long after our observation period [e.g., *Miyama et al.*, 2006].

Because our measurements are made in the Earth's reference frame and there is a nonzero zonal mean flow, we do this analysis in two steps. We make a preliminary determination of the wave type using measurements of the period and vertical wave number in the Earth's (and ship's) reference frame (section 4.1), then we refine our estimate of the period to account for the Doppler shift (section 4.2).

In the present data set, dependence on depth and time (stations T1 and T2) is captured much more thoroughly than is horizontal variability (transects M1–M4, Z). We therefore use the depth-time structure to

deduce the wave parameters and reserve measurements of meridional variability (M1–M3) for consistency checks (section 4.3).

4.1. Time and Depth Dependences Observed in the Earth's Reference Frame

We focus on the depth range $-576\ \mathrm{m} < z < -324\mathrm{m}$, shown on Figures 2 and 3b by horizontal lines. We refer to this as the wave layer. This particular layer is chosen for analysis because

1. U and N were relatively uniform with depth (Figure 2);
2. the layer thickness was about one half the vertical wavelength of the feature we are interested in. The boundaries of the layer were adjusted to make this relationship exact, simplifying the analysis.

To identify the wave type, we locate the observed oscillation on the nondimensional wave number plane k^*-m^* (Figure 4; see Appendix A for definitions). The first step is to estimate the quantities that combine to form m^* (A5), those being N^2, β, and the vertical wave number and period of the wave. The mean value of N in the wave layer was $3.37\times10^{-3}s^{-1}$, with standard error 1% (which we consider negligible), and the equatorial value of β is $2.28\times10^{-11}m^{-1}s^{-1}$. Estimating the wave number and period requires more detailed analysis.

The two solid lines on Figure 3b, being the most clearly defined phases, are used to estimate the wave number and period. Those lines are obtained as a least-squares fit to the local extrema of V on each phase (three for the first line, five for the second; visible on Figure 3b). Since the wave signal was clearest between approximately 14 and 24 November, we estimate the vertical half-wavelength, $\lambda_z/2$, as the vertical separation of the two lines during this interval. Because the slopes are slightly different, we also obtain a value for the uncertainty in the wavelength. The result is $\lambda_z=(505\pm75)\mathrm{m}$; hence the vertical wave number is $m=2\pi/\lambda_z=\ (1.24\pm0.18)\times10^{-2}\mathrm{m}^{-1}$.

Similarly, the wave period is estimated using the temporal separation of the solid lines at depths within the wave layer. The resulting period is $T_E=(22.25\pm3.25)$ days. The corresponding frequency is $\omega_E=2\pi/T_E=(3.27\pm0.48)\times10^{-6}$s. Here and throughout this paper, the subscript "E" indicates that the quantity is measured in the Earth's reference frame as opposed to that of the mean flow, a significant distinction that we will discuss in the next subsection. The subscript is not needed on the vertical wave number m, as its value is the same in both reference frames.

In what follows we compute several wave properties based on the estimates of m and ω_E described above. To estimate the uncertainties in these derived properties resulting from the uncertainties in m and ω_E, we use a Monte Carlo method. We assume that the central values of m and ω_E are the most reliable, and therefore model the probability distributions of those parameters as Gaussian. We first generate 10^5 Gaussian, quasi-random values for each of m and ω_E. The mean of each distribution is the estimate identified above, and the uncertainty is one standard deviation. The wave properties of interest are then computed for each of the 10^5 pairs of values for m and ω_E. Because the distribution of the derived quantity is in general non-Gaussian, the standard deviation is not a good measure of uncertainty. Instead, we identify the range of uncertainty as the inner four sextiles, i.e., we

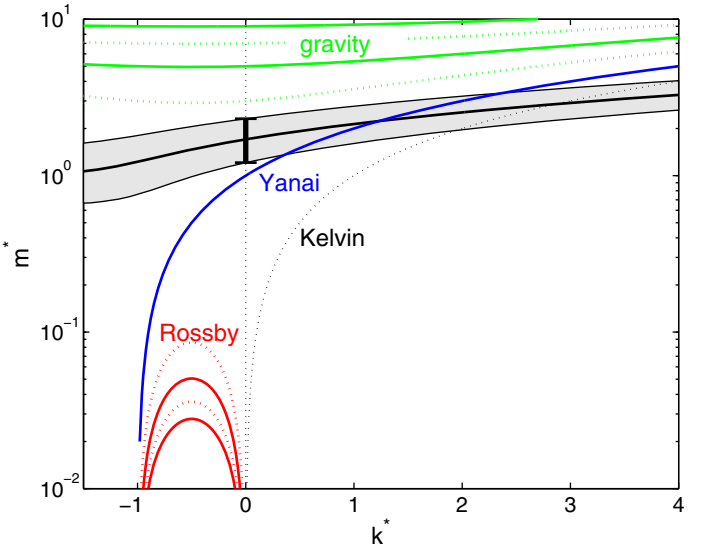

Figure 4. Dispersion relation on the k^*-m^* plane, defined in (A5), for linear, vertically propagating waves in a uniformly stratified environment with zero mean flow [e.g., *Gill*, 1982]. Solid (dotted) curves indicate even (odd) modes, characterized by purely meridional (zonal) velocity at the equator. The bar at $k^*=0$ (which coincides with the special case of zero Doppler shift; see (2)) shows the graphical estimate of m_E^* and its range of uncertainty. The grey band indicates the range of m^* as a function of k^* accounting for the Doppler shift.

exclude the largest one-sixth and the smallest one sixth of the values. In the special case of a Gaussian distribution, this range is very close to one standard deviation. In the case of m_E^* (the scaled wave number m^* measured in the Earth's reference frame), the inferred value is 2.85 and the range of uncertainty is (1.64,4.59).

This result can be interpreted in the framework of the linear theory for equatorially trapped waves (Figure 4; see Appendix A for details). The modes with purely meridional velocity at the equator are the Yanai wave and the Rossby and gravity waves of even order. Figure 4 shows the dispersion relations for these waves as solid curves. Also shown are the estimated error bounds on m_E^* (error bar located at $k^*=0$). The range of m_E^* is within the band $0.05 < m^* < 5$ where no even mode except the Yanai wave exists. We therefore provisionally identify the observed disturbance as a Yanai wave.

At this stage it is also useful to estimate the meridional trapping scale using (A9). The result is $L_{eq}=0.98$ (0.92,1.06) degrees latitude, or 109 (102,118) km. We will also have use for the amplitude of the meridional velocity, read directly from Figure 3b as $v_0 \approx 0.10 \pm 0.02 \mathrm{m/s}$.

4.2. The Doppler Shift

Because the mean zonal flow in the wave layer was nonzero and the ship was stationary, the frequency we observed is not the intrinsic frequency, i.e., the frequency in a reference frame moving with the mean flow, to which the standard linear theory applies. If a wave's frequency in the Earth's reference frame is ω_E, then its intrinsic frequency is

$$\omega=\omega_E-kU_p, \tag{1}$$

in which U_p is the velocity that accomplishes the Doppler shift. U_p is related to the mean velocity $\bar{U}$ shown in Figure 2a, but is reduced to 75% of this value to account for the imperfect projection of the mean flow onto the meridional structure of the Yanai wave (see Appendix B for details).

We have suggested in section 4.1 that the observed disturbance was a Yanai wave based on the frequency and vertical phase velocity measured in the Earth's reference frame, and have used that assumption in computing U_p. We are now able to check for self-consistency using values appropriate to the reference frame of the mean flow. To show the Doppler frequency shift on the k^*-m^* plane, we substitute $k=k^*\beta/\omega$ in (1) and solve the resulting quadratic equation for ω:

$$\omega=\omega_E\left(\frac{1}{2}\pm\sqrt{\frac{1}{4}-\frac{\beta U_p}{\omega_E^2}k^*}\right). \tag{2}$$

Requiring that $\omega \to \omega_E$ when $U_p \to 0$, we choose the plus sign. From this, we obtain the intrinsic value of m^* as a function of k^*:

$$m^*=m_E^*\left(\frac{1}{2}-\frac{\beta U_p}{\omega_E^2}k^*+\sqrt{\frac{1}{4}-\frac{\beta U_p}{\omega_E^2}k^*}\right). \tag{3}$$

At each k^*, the Monte Carlo method described above was used to obtain the median and range of m^*. The resulting range is shown by the grey band on Figure 4. Despite added variation due to the Doppler shift, the band of possible values of m^* crosses only the dispersion curve of the Yanai wave. We conclude that the observed wave properties are consistent with the Yanai dispersion relation in the reference frame of the mean flow in the wave layer.

4.3. Consistency Check: The Meridional Trapping Scale

The meridional sections M1–M4 yielded independent estimates of the trapping scale L_{eq} which may be compared with that inferred above from the time-depth dependence. The squared meridional velocity of a Yanai wave varies as

$$\frac{\overline{v^2}}{v_0^2}=\exp\left(-\frac{y^2}{L_{eq}^2}\right)=1-\frac{y^2}{L_{eq}^2}+O\left(\frac{y^4}{L_{eq}^4}\right), \tag{4}$$

Here $\overline{v^2}$ is the mean-square average of the meridional velocity computed using (A14) with $a=b=v$ and $\ell=1$. The variable v_0 is the amplitude of v at the equator.

To fit the observed meridional velocity for each transect M1–M4, we compute the symmetric part of the meridional velocity by averaging positive and negative latitudes: $v_s(y)=[v(y)+v(-y)]/2$. We then compute the root-mean-square average $\overline{v_s^2}$ over the wave layer, whose thickness is one half the inferred vertical wavelength. The resulting curve (Figure 5, solid curves) is fitted to a polynomial function:

$$\frac{\overline{v_s^2}}{v_0^2}=1+\sum_{n=1}^{4}a_n y^{2n}, \tag{5}$$

using a least-squares fit over the latitude range $[0, 0.75]$ degrees (Figure 5, dashed curves) to determine the constants a_n.

The trapping scale is then estimated as $\sqrt{-1/a_1}$. The values obtained for the four meridional transects are 1.11, 0.96, 1.13 and 3.74°, respectively. The result for M4 is an outlier; evidently, the meridional velocity was dominated by phenomena other than equatorially trapped waves during that transect. (Recall that M4 was located 1000 km east of the other three meridional transects.) The trapping scale for M2, the transect closest to the time when the wave signal was clearest, is very close to the estimated value of 0.98° (section 4.1). Trapping scales for transects M1 and M3, during which the wave signal was much less clear, lie outside the range of uncertainty for L_{eq}, though not by far (Figure 6).

If we repeat the curve-fitting assuming a second-mode Rossby or gravity wave, the resulting estimate of the trapping scale is larger by a factor $\sqrt{5}$, so that all transects give values far from our estimate. We conclude that the observed meridional structure is consistent with a Yanai wave with the inferred frequency and vertical wave number.

5. Inferred Properties of the Dominant Yanai Wave

The assumption that the observed oscillations result from a Yanai wave packet with the temporal/vertical structure inferred above allows us to estimate various other wave parameters of interest using the Yanai wave dispersion relation (A4) and its generalized form (B3). These include both first-order quantities (the zonal scale and the phase and group velocities; section 5.1) and second-order transports (energy flux, heat flux and Stokes drift velocity; sections 5.2–5.4). In addition to their potential effects on the mean state, the second-order quantities each furnish an independent measure of wave amplitude that can be compared with existing measurements of internal waves and related phenomena. Numerical values are summarized in Table 2, along with the uncertainty ranges derived using the Monte Carlo method described above.

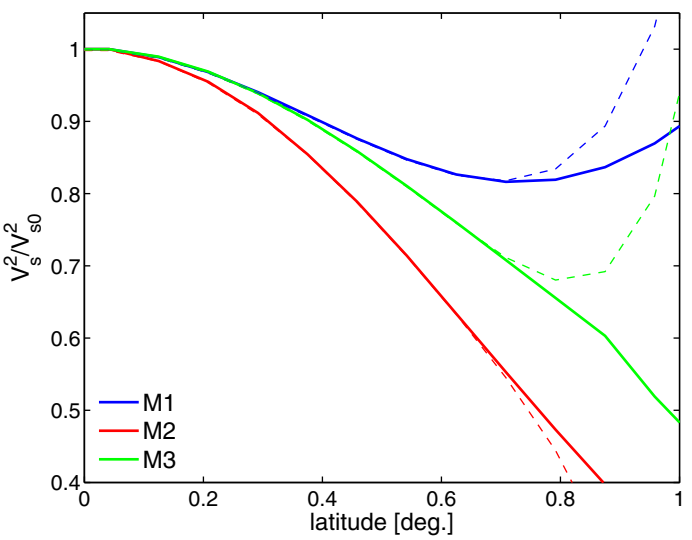

Figure 5. Mean square meridional velocity profiles for M1–M3. Averages are computed in the wave layer using the symmetric part of *v*. Solid curves indicate three different transects, color-coded as in the legend. Dashed curves show the polynomial fit (5) for each transect.

5.1. First-Order Spatiotemporal Structure

We first obtain the zonal wave number *k* using (B3), with uncertainty range given by the Monte Carlo method (Figure 7a). The estimated value $k=7.76\times10^{-6}\mathrm{m}^{-1}$ corresponds to a zonal wavelength of 810 km.

We note that the zonal structure we infer here is different from previous observations of Yanai waves in the Indian Ocean in that it implies eastward phase propagation. For example, the observations of *Sengupta et al.* [2004] indicate westward phase propagation. According to our Monte Carlo uncertainty analysis, there is only a 7% probability that the

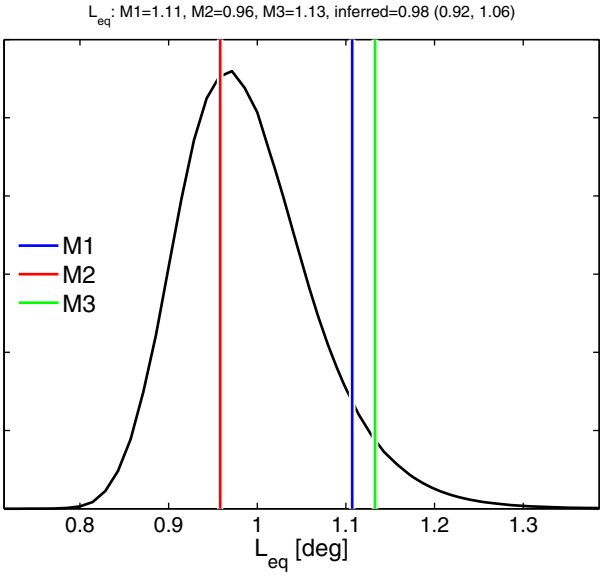

Figure 6. Probability distribution of the meridional trapping scale for the linear Yanai wave inferred in section 4.1. Variability corresponds to the uncertainty in observational estimates of m and ω_E. Superimposed are three vertical lines showing direct estimates from meridional transects M1, M2, and M3.

wave number is negative. The most likely interpretation is therefore that the wave described here had eastward phase propagation.

Using this estimate of k in (1), we can now obtain the Doppler-shifted frequency and period (Figure 7b). The period is shifted from $T_E = 22.2$ days in the Earth frame to $T = 19.4$ days in the mean flow frame.

The zonal phase speed $c_x = \omega/k$ is of particular interest because it allows us to quantify the wave steepness. Defined as v_0/c_x (roughly the ratio of the maximum meridional excursion to one quarter the zonal wavelength λ_x, or the ratio of nonlinear terms to time derivatives in the momentum equations), the steepness is here equal to 0.21. The linearization underlying our plane wave model (Appendix A) is valid inasmuch as this quantity is $\ll 1$.

The zonal phase speed also shows that the observed wave is likely to have a critical surface surrounding the core of the Wyrtki jet (cf. Figures 2a and 3a). The group velocity (c_{gx}, c_{gz}) in the wave layer is directed downward and to the east, consistent with a Yanai wave with upward phase propagation.

5.2. The Vertical Energy Flux

The downward flux of kinetic energy is calculated in terms of v as described in Appendix A, giving

$$-\overline{pw} = \frac{\rho_0}{2} m\omega \frac{\omega^2}{N^2} y^2 |\hat{v}|^2. \tag{6}$$

Table 2. Parameter Values for the Yanai Wave Inferred From the Observed Time-Depth Dependence[a]

Parameter	Unit	Value	Uncertainty
λ_z	m	505	(430,580)
T_E	days	22.2	(19.0,25.5)
T	days	19.4	(16.3,23.9)
K	$10^{-6}\mathrm{m}^{-1}$	7.76	(2.86,12.4)
λ_x	km	810	(451,1580)
L_{eq}	km	109	(102,118)
c_{xE}	m/s	0.421	(0.263,0.762)
c_x	m/s	0.484	(0.324,0.825)
c_z	m/d	26.1	(21.0,31.9)
c_{gxE}	m/s	0.126	(0.097,0.149)
c_{gx}	m/s	0.188	(0.160,0.211)
c_{gz}	m/d	−18.1	(−23.5,−12.8)
$-\overline{pw}_{max}$	$\mathrm{mW/m}^2$	1.30	(0.56, 2.39)
$-\langle pw \rangle$	$\mathrm{mW/m}^2$	0.16	(0.07,0.29)
$-d\overline{vT}/dy_{max}$	K/month	0.339	(0.195, 0.512)
u_{Smax}	$10^{-2}\mathrm{ms}^{-1}$	1.82	(1.15, 2.67)
$-w_{Smax}$	$10^{-5}\mathrm{ms}^{-1}$	1.97	(1.18,3.09)

[a]The subscript "E" indicates evaluation in the Earth's reference frame. The range of uncertainty is the inner four sextiles, except in the cases of T_E and λ_z, whose uncertainties are estimated graphically (see section 4.1).

This flux vanishes at the equator and is downward elsewhere, reaching the extremal value $-\overline{pw}_{max}$ at $y = \pm L_{eq}$.

As a standard of comparison for the magnitude of the observed waves, we use the energy flux due to near-inertial waves, the dominant carrier of wind energy to the deep ocean at midlatitudes. A global view of this flux has been given by *Alford* [2001, 2003]. Those studies show transfers of wind energy to near-inertial waves ranging from 5 to 50 $\mathrm{mW/m}^2$ in winter in Western boundary currents, and down to 0.1 $\mathrm{mW/m}^2$ or less in Eastern basins [*Alford*, 2001, Figure 4]. In the tropical Indian Ocean, fluxes of 1–4 $\mathrm{mW/m}^2$ are common, and often increase to 10 $\mathrm{mW/m}^2$ in the energetic zone south of Sri Lanka.

Also, two direct observations of near-inertial waves have been made at 8S in the Indian Ocean. *Cuypers et al.* [2013] observed near-inertial wave packets at 8S, 67.5E excited by a tropical storm. Their estimate

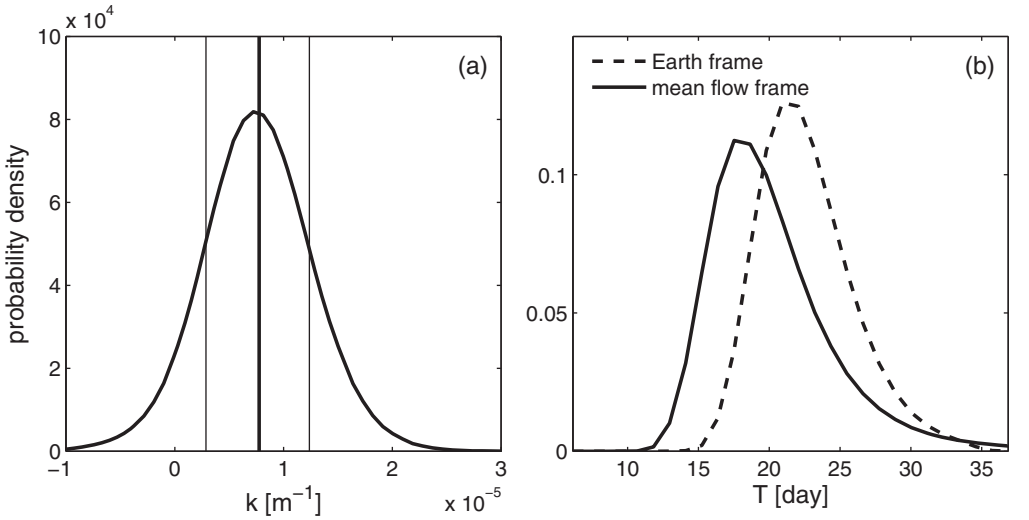

Figure 7. (a) Probability distribution function for the zonal wave number of the linear Yanai wave inferred from the time-depth sections T1 and T2. Vertical lines show the estimated value and the uncertainty range. (b) Probability distribution functions for the period of the linear Yanai wave inferred from the time-depth sections T1 and T2. Dashed and solid curves correspond to values as measured in the Earth's reference frame and in a reference frame stationary with respect to the mean flow in the wave layer, respectively.

of the maximum downward energy flux was 2 mW/m^2, with similar values extending from 100 to 400 m depth. Similar observations at 8S, 80.5E showed a wave packet at 60–130 m depth carrying a downward energy flux of 1.9 mW/m^2 and a second, much weaker signal below 180 m carrying 0.17 mW/m^2 [*Soares et al*., 2014].

Our estimate for the maximum downward energy flux due to the Yanai wave, 1.30 (0.56, 2.39) mW/m^2, is similar to that due to the inertial wave events observed at 8S [e.g., *Cuypers et al*., 2013] and is within the range of values found in the tropical Indian Ocean by *Alford* [2001].

The downward energy flux driven by Yanai waves in the equatorial Pacific, averaged over two years, was estimated by *Eriksen and Richman* [1988] to be 0.15 mW/m^2 (reading from their Figure 8 and dividing by 4 to account for differences in the definition). Following *Eriksen and Richman*, we define a characteristic value for the energy flux per unit horizontal area in the equatorial waveguide:

$$-\langle pw\rangle_{peak} = -\frac{1}{2L_{eq}}\int_{-\infty}^{\infty}\overline{pw}\,dy = \frac{\sqrt{\pi}}{8}\frac{\rho_0}{\beta}S_m\frac{\omega^3}{N}v_0^2 = 1.50\ \ (0.69, 2.88)\ \ \mathrm{mW/m^2}, \tag{7}$$

where S_m is the sign of m. A dominant factor explaining the order-of-magnitude difference is likely to be the difference in averaging: *Eriksen and Richman*'s estimate is an average over two years whereas ours is the peak value in a wave event. For a more meaningful comparison, we convert our estimate to a long-time average. For want of a longer time series in this depth range, we estimate the long-time average as follows. We approximate the envelope of the wave packet such that the energy flux is proportional to e^{-t^2/τ^2}, and assume that similar events recur at intervals τ_r. The long-time average is then the peak value times $\sqrt{\pi}\tau/\tau_r$. Based on Figure 3, we estimate $\tau \approx$ 10 days. The wavelet analyses of *David et al*. [2011] suggest that a similar event happens 1–3 times per year, in which case $\sqrt{\pi}\tau/\tau_r \sim 0.1$. Multiplying this ratio onto $\langle pw\rangle_{peak}$ results in a time-averaged energy flux $\langle pw\rangle = 0.16$ mW/m^2, statistically indistinguishable from the *Eriksen and Richman* [1988] estimate despite the difference in locale.

To summarize, the downward energy flux due to the Yanai waves observed here is similar to that found for individual instances of wind-driven near-inertial waves at 8S in the Indian Ocean, and to seasonally averaged values in the relatively energetic zone near Sri Lanka. The flux is similar to that carried by Yanai waves deep in the Pacific [*Eriksen and Richman*, 1988] when differences in averaging are accounted for.

5.3. The Meridional Heat Flux

Using (A12), we find that downgoing Yanai waves carry an equatorward heat flux:

$$\rho_0 c_p \overline{vT} = -\frac{1}{2}\frac{\rho_0 c_p}{\alpha g} m\omega y |\hat{v}|^2, \tag{8}$$

where α is the thermal expansion coefficient, g is the acceleration due to gravity, c_p is the specific heat at constant pressure, and $T = b/\alpha g$ is the perturbation temperature. (We have neglected the potential influence of salinity gradients.) The convergence of this flux is:

$$-\frac{\partial}{\partial y}\overline{vT} = \frac{1}{2}\frac{\rho_0 c_p}{\alpha g} m\omega v_0^2 \left(1 - 2\frac{y^2}{L_{eq}^2}\right) \exp\left(-\frac{y^2}{L_{eq}^2}\right). \tag{9}$$

Comparison of (9) with (6) at $y = 0$ reveals that the flux due to waves with downward (upward) energy flux converges (diverges) at the equator. Previous researchers have evaluated a term equivalent to (9) in model output and field observations, and we will compare the value implied by our observations with these existing results. The effect of the wave on the mean temperature is not addressed here because a second-order vertical advection term, which we cannot estimate with the present data, may partly or wholly balance the meridional heat flux (see Appendix A).

The mechanism for the meridional heat flux convergence is shown schematically in Figure 8. The phase relationship between the temperature perturbation and the meridional velocity is such that, provided that the phase progression is upward, warm (cool) anomalies are always carried equatorward (poleward). If phase motion is downward (energy flux upward), the flux convergence is opposite, tending to cool the equator. Bottom reflection therefore leads to destructive interference, and the vertical mode structure produced by multiple reflections generates no net heat flux.

For the observed wave, (9) gives a flux convergence rate of order 0.33 K/month. An interesting standard for comparison is tropical instability waves (TIWs) in the Pacific and Atlantic basins, which have been studied extensively and which are known to exhibit a convergent meridional heat flux and to coincide with a warming of the equatorial cold tongue. The comparison is also pertinent because tropical instability waves often have spatial structure resembling a Yanai wave [e.g., *Lyman et al*., 2007; *Shinoda*, 2010]. Using surface drifters, *Hansen and Paul* [1984] estimated this convergence as ~3 K/month (graphically differentiating the meridional temperature flux in their Figure 6b). The order-of-magnitude difference is actually less than one would expect based on the scale of the wave. The convergence rate is, to first order, proportional to v_0^2, and in the *Hansen and Paul* [1984] observations v_0^2 exceeded the present value by a factor 36 (based on their Figure 5b). Although many factors contribute to the difference, an obvious one is nonlinear saturation in the large-amplitude TIWs, which would make the present extrapolation from linear theory an overestimate.

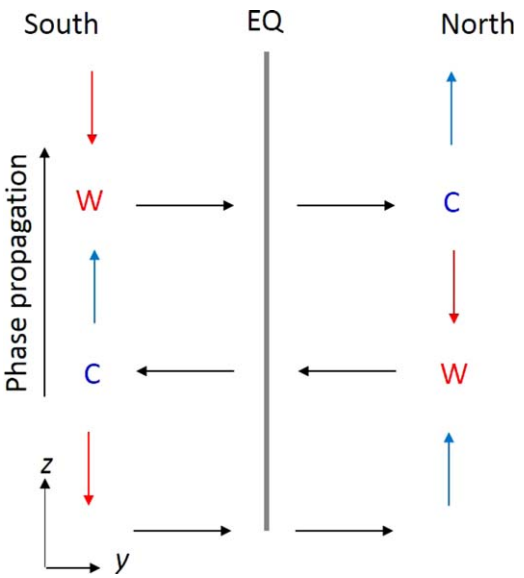

Figure 8. Schematic of the y – z structure of a Yanai wave with upward phase propagation, illustrating the mechanism of net flux convergence at the equator. Layers of vertical motion alternate with layers of meridional motion. As the pattern moves upward, temperature anomalies created by the vertical motions are advected by the meridional flow so that, at each phase, warm (cool) water is carried toward (away from) the equator. If the phase propagation were downward (energy propagation upward), the heat flux would be reversed so as to carry cool water toward the equator.

Nagura et al. [2014] have analyzed equatorial heat fluxes in the upper 200 m using model results and observations from an array of moorings at 1.5S, 0 and 1.5N latitude and 80.5E and 90E longitude [*McPhaden et al*., 2009]. A convergent flux at the equator was shown to be associated with Yanai

waves. The flux convergence peaked around 2.5 K/month in the seasonal pycnocline (100–150 m depth), then decreased with depth, reaching 0.15 K/month at 200 m. Our estimate of the convergence rate, 0.33 K/month, is toward the low end of the range of values found by Nagura et al, as might be expected due to the difference in the depth range. Another caveat to this comparison is that *Nagura et al*. computed $-\overline{v\partial T/\partial y}$, whereas we estimate $-\overline{\partial(vT)/\partial y}$. In the present, idealized theory these expressions are equal, but the difference could be important in the more realistic model used by *Nagura et al*.

5.4. The Stokes Drift

For the Yanai plane wave the Stokes drift vector is

$$\vec{u}_S = \left(\frac{|m|}{m}\frac{N}{\omega}, 0, -1\right)\left[\frac{m\omega}{N^2}\frac{v_0^2}{2}\left(1-2\frac{y^2}{L_{eq}^2}\right)\exp\left(-y^2/L_{eq}^2\right)\right]. \tag{10}$$

The Stokes drift is parallel to the group velocity vector as given by (A7); the meridional component is everywhere zero; the zonal and vertical components have the same meridional distribution; and the meridional integral of each vanishes. In the present case, the maximum zonal component, occurring at the equator, is $1.82\times10^{-2}\mathrm{ms}^{-1}$, or $\sim$ 1.6 km/d to the east. For comparison, the Stokes drift due to surface waves is typically $O(10^{-1})\mathrm{ms}^{-1}$ but ranges up to $O(1)\mathrm{ms}^{-1}$ in extreme conditions [e.g., *Smith et al*., 2013]. The vertical Stokes drift at the equator is $1.97\times10^{-5}ms^{-1}$, or 1.7 m/d, directed downward. Secondary extrema exist at $y=\pm130km$, where the Stokes drift is $-e^{-1}$ times the equatorial value.

6. Summary and Discussion

Our observations reveal a vertically propagating meridional velocity signal in the upper thermocline of the central equatorial Indian Ocean during late October–November 2011. In a $\sim$300 m-thick layer beneath the surface currents and seasonal pycnocline, both the mean zonal current and the mean stratification were nearly independent of depth. Within this layer, we are able to compare the observations with the classical theory of vertically propagating equatorial waves, and thereby to identify the signal as a Yanai wave beam. The theory has been used to compute various space and time scales of interest in both the Earth's reference frame and that of the mean flow, and to estimate the Stokes drift and the fluxes of heat and energy carried by the wave.

Estimation of wave parameters has necessitated consideration of the Doppler shift due to the projection of the mean zonal current onto the meridional wave structure (Appendix B). The Doppler-shifting mean current identified here is unlikely to be generic. Our observations were made during the season when the Wyrtki jet and its undercurrent are typically strong [e.g., *Luyten and Roemmich*, 1982; *Nagura and McPhaden*, 2010]. The zonal current we observed (Figure 3a) varied considerably, though on a time scale too long to affect our calculations.

A preliminary backward ray tracing using the mean buoyancy-frequency profile and the time history of upper level currents measured at the 0N, 80.5E RAMA mooring suggests that the observed wave could have been forced roughly 10° to the west and 3 months prior to our observations. From mid-July to early September, the TropFlux data [*Kumar et al*., 2013] show three bursts of meridional wind stress on the equator between 65E and 75E, with separations of roughly 18 and 28 days. We cannot, however, connect these winds to our observations with any degree of certainty. The vertical and temporal scales of the zonal surface current and undercurrent are comparable to the scales of the observed wave, bringing the validity of the ray-tracing approximation into question. In addition, the current velocities occasionally exceed the zonal group velocity of the wave. Even when critical layers are not encountered, small uncertainties in the current amplitudes (such as might be due to the unknown longitudinal dependence, for instance) can lead to widely divergent predictions.

The possibility of an instability generation mechanism cannot be ruled out. *David et al*. [2011] noted robust 28 day variability of antisymmetric sea-surface-height anomalies in the central equatorial Indian Ocean, and calculated positive barotropic conversion in the region from surface currents. They did not, however, provide a rationale for the observed periodicity of the Yanai-wave motions. A confident estimate of our observed wave's origin would require three-dimensional process modeling.

Our estimated vertical energy flux is comparable to that driven by Yanai waves in the equatorial Pacific [*Eriksen and Richman*, 1988], and to that due to midlatitude near-inertial waves. Vertically propagating Yanai waves do not carry a vertical heat flux, but they can flux heat meridionally toward the equator. *Nagura et al*. [2014] note that equatorial heat flux convergence does not occur in a 1.5-layer model and explain the observed convergence based on the full equations of motion. In the theory used here, equatorial flux

convergence emerges simply as a consequence of vertical propagation and is readily estimated in terms of measurable wave properties (equation (9)). This is consistent with *Nagura et al.*'s finding that convergence occurs in a basin-scale model only when multiple baroclinic modes are included (since many modes are needed to represent vertical propagation) [e.g., *Miyama et al.*, 2006].

We emphasize that the convergence of the meridional heat flux is only one contribution to the wave's effect on the ambient temperature (see Appendix A). Estimation of the full effect of second-order wave processes on the mean ocean state will require further studies accounting for boundaries, turbulent dissipation and surface forcing.

Appendix A: Review of Small-Amplitude Theory for Vertically Propagating Yanai Waves

Here we will briefly review the modal structure of linear, vertically propagating, plane Yanai waves as developed by *Matsuno* [1966] and *Lindzen and Matsuno* [1968]. The theory employs the Boussinesq equations on the equatorial β-plane, where the Coriolis parameter is linearized about the equator as $f=\beta y$. Zonal, meridional and vertical (upward) coordinates are x, y and z, while u, v and w are the corresponding components of the perturbation velocity. The theory assumes a motionless background field and a background buoyancy that is locally linear in z, such that the buoyancy frequency (N) can be considered constant over the vertical scale of the wave. The dynamical equations are expanded in terms of an amplitude parameter $\epsilon=u_0/c_x$, where u_0 is the scale of the perturbation zonal velocity and c_x is the zonal phase speed (defined below). We focus on the lowest order (i.e., linear) solution. In the parameter range of the observed Yanai wave, $u_0 \approx v_0$, the meridional velocity amplitude on the equator, making v_0/c_x a useful measure of the wave's linearity.

The linear equations are

$$\begin{gathered} u_t - fv + \pi_x = 0; \quad v_t + fu + \pi_y = 0; \\ -b + \pi_z = 0; \quad b_t + N^2 w = 0; \\ u_x + v_y + w_z = 0; \end{gathered} \tag{A1}$$

where b is the buoyancy perturbation, and $\pi=p/\rho_0$ is the pressure perturbation scaled by a constant characteristic density ρ_0. Consistent with the β-plane approximation, we require that all variables remain bounded as $y \to \pm\infty$.

For all wave classes except the Kelvin wave (which we do not consider here), (A1) is combined into a single equation for v. For a vertically propagating plane wave, v has the normal mode form

$$v = \left(\hat{v}(y) e^{i\Phi}\right)_r, \tag{A2}$$

where $\hat{v}(y)$ is the structure function describing equatorial trapping of the meridional motion, and the subscript "r" denotes the real part. The phase function is given by

$$\Phi = kx + mz - \omega t, \tag{A3}$$

where k and m are zonal and vertical wave numbers, respectively, ω is the radian frequency and t is the time.

For the Yanai wave solution, spatial and temporal scales are related by the dispersion relation

$$k = \frac{|m|\omega}{N} - \frac{\beta}{\omega}. \tag{A4}$$

Alternatively, we can define the nondimensional wave numbers [e.g., *Gill*, 1982]

$$k^* = k\frac{\omega}{\beta} \quad \text{and} \quad m^* = \frac{m\omega^2}{\beta N}, \tag{A5}$$

in which case the dispersion relation is simply

$$k^* = m^* - 1. \tag{A6}$$

The vertical and zonal phase speeds are $c_z=\omega/m$ and $c_x=\omega/k$, and the group velocity vector is

$$\vec{c}_g = c_z \frac{|m^*|}{|m^*|+1}\left(\frac{|m|}{m}\frac{N}{\omega}, 0, -1\right). \tag{A7}$$

The meridional structure function for the Yanai wave has the Gaussian form

$$\hat{v}(y) = v_0 e^{-y^2/2L_{eq}^2}, \tag{A8}$$

where L_{eq} is the meridional trapping scale, given by

$$L_{eq} = \sqrt{\frac{N}{\beta|m|}}. \tag{A9}$$

Zonal and vertical velocity components, as well as buoyancy and pressure perturbations, have the modal form (A2), but with separate meridional structure functions related to $\hat{v}$ by polarization relations:

$$\hat{u} = i\frac{\omega|m|}{N}y\hat{v}, \tag{A10}$$

$$\hat{w} = -i\frac{m\omega^2}{N^2}y\hat{v}, \tag{A11}$$

$$\hat{b} = -m\omega y\hat{v}, \tag{A12}$$

$$\hat{p} = i\rho_0\omega y\hat{v}. \tag{A13}$$

Certain quadratic products of the linear fields (including energy flux and buoyancy flux) have nonvanishing period (or wavelength) averages. The half-wave-cycle average (designated by an overbar) of a quadratic term is evaluated using the general formula

$$\overline{ab} = \frac{1}{\ell\pi}\int_0^{\ell\pi} ab\ d\Phi = \frac{1}{2}(\hat{a}\hat{b}^*)_r; \quad \ell = 1, 2, 3, \ldots, \tag{A14}$$

where a and b are any two perturbation fields with meridional structure functions $\hat{a}$ and $\hat{b}$, the asterisk indicates the complex conjugate. The combination $\overline{ab}$ is averaged over the phase Φ (or, equivalently, x, z, and/or t), but it remains a function of y. Note that the result is independent of the integer ℓ. In the present analyses, applicability of (A14) to the observations is ensured by adjusting the boundaries of the wave layer (section 4.1) to encompass one half the vertical wavelength $\lambda_z = 2\pi/m$, equivalent to setting $\ell = 1$.

Two quadratic terms of particular interest are the average vertical energy flux and the average meridional buoyancy flux. These are are, respectively,

$$\overline{pw} = -\frac{\rho}{2}m\omega\frac{\omega^2}{N^2}y^2|\hat{v}|^2, \tag{A15}$$

$$\text{and} \quad \overline{bv} = -\frac{1}{2}m\omega y|\hat{v}|^2. \tag{A16}$$

The meridionally varying buoyancy flux described by (A16) can in principle lead to net heating or cooling. This is not necessarily the case, however, as the meridional flux can be balanced exactly by a second-order vertical velocity advecting the background density field (the second-order w being induced by the linear v paralleling the meridionally tilted isopycnals). The nonacceleration theorem [e.g., *Holton*, 1974; *Andrews and McIntyre*, 1976; *Boyd*, 1976; *McPhaden et al.*, 1986; *Ascani et al.*, 2010] implies that this must be the case in the adiabatic system that we consider. In realistic conditions, however, dissipation and wave transience can break the balance, allowing (A16) to contribute to near-equatorial heating. Estimating the magnitude of any net heating is beyond the scope of this work, but in section 5.3 we compare the magnitude of horizontal heat flux convergence implied by (A16) with measurements made by previous researchers of similar terms in model output and field observations.

Appendix B: Estimation of the Doppler Shift

Durland et al. [2011] showed that the background zonal currents can affect the dispersion relation of an equatorial wave through the Doppler shift, modification of the background potential vorticity field, and modification of the effective deformation radius. After an iterative solution, we determine that the observed Yanai wave is closer

to the gravity wave limit than to the Rossby wave limit, and we thus expect the latter two effects to be small compared to the Doppler shift. The effective Doppler-shifting current is equal to the projection of the background current structure onto the vertical and meridional structures of the wave's total (potential plus kinetic) energy field [*Proehl*, 1990; *Durland et al.*, 2011]. For a Yanai wave approaching the gravity wave limit, a considerable fraction of the total energy field is associated with the pressure and zonal velocity, both of which peak at one deformation radius off the equator. Because the background zonal current peaks on the equator, we expect the effective Doppler shifting current to be smaller than the measured zonal current on the equator. Because we don't know the meridional dependence of U during stations T1 and T2, we use an average of the meridional structures measured during transects M1 and M2 to compute the above projection.

Assuming that the wave is indeed a Yanai wave (as is argued in section 4.1), the meridional dependence of the total wave energy (kinetic plus potential) is proportional to

$$E(y)=\left(1+2\frac{\omega^2 m^2}{N^2}y^2\right)e^{-y^2/L_{eq}^2}. \tag{B1}$$

Computation of this profile requires a value of ω, which is itself affected by the Doppler shift, so an iterative solution is necessary.

An estimate of the background zonal velocity $U(y, z)$ is obtained by averaging the ADCP observations from the meridional transects M1 and M2. The resulting velocity is then averaged vertically over the wave layer to produce a meridional profile $U_m(y)$. This profile is projected onto the Yanai wave energy profile $E(y)$:

$$U_p=\frac{\int_{-y_2}^{y_2}E(y)U_m(y)dy}{\int_{-y_2}^{y_2}E(y)dy}. \tag{B2}$$

The limit of our meridional transects is $y_2=222$km and this latitude range captures most of $E(y)$.

Estimation of the Doppler shift via (1) also requires a value for the zonal wave number k. This is obtained as a solution of

$$U_p\left(1+\frac{mU_p}{N}\right)k^2-\omega_E\left(1+2\frac{mU_p}{N}\right)k+\omega_E^2\frac{m}{N}-\beta=0, \tag{B3}$$

a generalization of the Yanai wave dispersion relation (A4) accounting for the Doppler shift due to the uniform mean current U_p. The solution is chosen so that (A4) is recovered in the limit $U_p \to 0$.

Equations (1), (B2), and (B3) are iterated, with ω_E as the starting value for the frequency. The iteration requires only a few steps to converge. The result is a value for the projection factor

$$F=\frac{U_p}{U_m(0)}=0.74. \tag{B4}$$

The mean zonal velocity for the stations T1 and T2 (Figure 2) is multiplied by this factor to obtain $U_p=-0.062\mathrm{m/s}$.

Acknowledgments

Thanks to Alexander Perlin and Elizabeth McHugh for data processing assistance, to Aurélie Moulin for a critical reading, and to the captain and crew of the R/V Revelle. We are indebted to François Ascani for pointing out the potential advective effect of the wave-induced mean flow. Comments from an anonymous reviewer are also appreciated. Funding for this project has been provided by the Office of Naval Research (N001–10-7–2098), the National Science Foundation (grants OCE1030772, OCE1129419, OCE1336752, and OCE1059055), and the National Aeronautics and Space Administration (grants NNX13AE46G and NNX10AO93G). Data from the Dynamo project are archived at: https://www.eol.ucar.edu/field_projects/dynamo. Software used in this study is available via direct request to the corresponding author.

References

Alford, M. (2001), Internal swell generation: The spatial distribution of energy flux from the wind to mixed layer near-inertial motions, *J. Phys. Oceanogr.*, *31*, 2359–2368.

Alford, M. (2003), Improved global maps and 54-year history of wind-work on ocean inertial motions, *Geophys. Res. Lett.*, *30*(8), 1424, doi: 10.1029/2002GL016614.

Andrews, D., and M. McIntyre (1976), Planetary waves in horizontal and vertical shear: The generalized Eliassen-Palm relation and the mean zonal acceleration, *J. Atmos. Sci.*, *33*, 2031–2048.

Ascani, F., E. Firing, P. Detrieux, J. McCreary, and A. Ishida (2010), Deep equatorial circulation induced by a forced-dissipated Yanai beam, *J. Phys. Oceanogr.*, *40*, 1118–1142.

Boyd, J. P. (1976), The noninteraction of waves with the zonally averaged low on a spherical earth and the interrelationships of eddy fluxes of energy, heat and momentum, *J. Atmos. Sci.*, *33*, 2285–2291.

Chatterjee, A., D. Shankar, J. P. McCreary, and P. N. Vinayachandran (2013), Yanai waves in the western equatorial Indian Ocean, *J. Geophys. Res. Oceans*, *118*, 1556–1570, doi:10.1002/jgrc.20121.

Cuypers, Y., X. L. Vaillant, P. Bouruet-Aubertot, J. Vialard, and M. J. McPhaden (2013), Tropical storm-induced near-inertial internal waves during the Cirene experiment: Energy fluxes and impact on vertical mixing, *J. Geophys. Res. Oceans*, *118*, 358–380, doi:10.1029/2012JC007881.

David, D. T., S. P. Kumar, P. B. M. S. S. Sarma, A. Suryanarayana, and V. S. N. Murty (2011), Observational evidence of lower frequency Yanai wave in the central equatorial Indian Ocean, *J. Geophys. Res.*, *116*, C06009, doi:10.1029/2010JC006603.
Dengler, M., and D. Quadfasel (2002), Equatorial deep jets and abyssal mixing in the Indian Ocean, *J. Phys. Oceanogr.*, *32*, 1165–1180.
d'Orgeville, M., B. L. Hua, and H. Sasaki (2007), Equatorial deep jets triggered by a large vertical scale variability within the western boundary layer, *J. Mar. Res.*, *65*, 1–25.
Durland, T. S., R. Samelson, D. Chelton, and R. DeSzoeke (2011), Modification of long equatorial Rossby wave phase speeds by zonal currents, *J. Phys. Oceanogr.*, *41*, 1077–1101.
Eriksen, C. (1982), Geostrophic equatorial deep jets, *J. Mar. Res.*, *40*, 143–157.
Eriksen, C., and J. Richman (1988), An estimate of equatorial wave energy flux at 9- to 90-day periods in the central Pacific, *J. Geophys. Res.*, *93*, 15,455–15,466.
Farrar, J., and T. Durland (2012), Wavenumber frequency spectra of inertiagravity and mixed Rossbygravity waves in the equatorial Pacific ocean, *J. Phys. Oceanogr.*, *42*, 1859–1881, doi:10.1175/JPO-D-11-0235.1.
Gill, A. (1982), *Atmosphere-Ocean Dynamics*, 662 pp., Academic, San Diego, Calif.
Hansen, D., and C. Paul (1984), Genesis and effects of long waves in the equatorial Pacific, *J. Geophys. Res.*, *89*, 10,431–10,440.
Holton, J. (1974), Forcing of mean flows by stationary waves, *J. Atmos. Sci.*, *31*, 942–945.
Holton, J., and R. Lindzen (1972), An updated theory for the quasi-biennial oscillation of the tropical stratosphere, *J. Atmos. Sci.*, *29*, 1076–1080.
Kelly, B. G., S. D. Meyers, and J. J. O'Brien (1995), On a generating mechanism for Yanai waves and the 25-day oscillation, *J. Geophys. Res.*, *100*, 10,589–10,612.
Kindle, J. C., and J. D. Thompson (1989), The 26- and 50-day oscillations in the western Indian Ocean: Model results, *J. Geophys. Res.*, *94*, 4721–4736.
Kumar, B. P., J. Vialard, M. Lengaigne, V. S. N. Murty, M. J. McPhaden, M. F. Cronin, F. Pinsard, and K. G. Reddy (2013), TropFlux wind stresses over the tropical oceans: evaluation and comparison with other products, *Climate dynamics*, *40*(7–8), 2049–2071.
Lindzen, R., and T. Matsuno (1968), On the nature of large-scale wave disturbances in the equatorial lower stratosphere, *J. Meteorol. Soc. Jpn.*, *46*, 215–220.
Luyten, J., and D. Roemmich (1982), Equatorial currents at semi-annual period in the Indian Ocean, *J. Phys. Oceanogr.*, *12*, 406–413.
Lyman, J., G. Johnson, and W. Kessler (2007), Distinct 17- and 33-day tropical instability waves in subsurface observations, *J. Phys. Oceanogr.*, *37*, 885–872.
Masumoto, H. H. Yukio, Y. Kuroda, H. Matsuura, and K. Takeuchi (2005), Intraseasonal variability in the upper layer currents observed in the eastern equatorial Indian Ocean, *Geophys. Res. Lett.*, *32*, L02607, doi:10.1029/2004GL021896.
Matsuno, T. (1966), Quasi-geostrophic motions in the equatorial area, *J. Meteorol. Soc. Jpn.*, *44*, 25–43.
McCreary, J. P. (1984), Equatorial beams, *J. Mar. Res.*, *42*, 395–430.
McPhaden, M., J. Proehl, and L. Rothstein (1986), The interaction of equatorial Kelvin waves with realistically sheared zonal currents, *J. Phys. Oceanogr.*, *13*, 1499–1515.
McPhaden, M. J., G. Meyers, K. Ando, Y. Masumoto, V. S. N. Murty, M. Ravichandran, F. Syamsudin, J. Vialard, L. Yu, and W. Yu (2009), RAMA: The research moored array for African–Asian–Australian monsoon analysis and prediction, *Bull. Am. Meteorol. Soc*, *90*, 459–480.
Miyama, T., J. P. McCreary, D. Sengupta, and R. Senan (2006), Dynamics of biweekly oscillations in the equatorial Indian Ocean, *J. Phys. Oceanogr.*, *36*, 827–846, doi:10.1175/JPO2897.1.
Moore, D. W., and J. P. McCreary (1990), Excitation of intermediate-frequency equatorial waves at a western ocean boundary: With application to observations from the Indian Ocean, *J. Geophys. Res.*, *95*, 5219–5231.
Moore, D. W., and S. G. H. Philander (1977), Modeling of the tropical ocean circulation, in *The Sea*, vol. 6, edited by E. Goldberg et al., pp. 319–362, Wiley-Interscience, N. Y.
Moum, J. N., et al. (2014), Air-sea interactions from westerly wind bursts during the November 2011 MJO in the Indian Ocean, *Bull. Am. Met. Soc.*, *95*, 1185–1199.
Nagura, M., and M. J. McPhaden (2008), The dynamics of zonal current variations in the central equatorial Indian Ocean, *Geophys. Res. Lett.*, *35*, L23603, doi:10.1029/2008GL035961.
Nagura, M., and M. J. McPhaden (2010), Wyrtki jet dynamics: Seasonal variability, *J. Geophys. Res.*, *115*, C07009, doi:10.1029/2009JC005922.
Nagura, M., Y. Masumoto, and T. Horii (2014), Meridional heat advection due to mixed Rossby-gravity waves in the equatorial Indian Ocean, *J. Phys. Oceanogr.*, *44*, 343–358.
Ogata, T., H. Sasaki, V. S. N. Murty, and M. S. S. Sharma (2008), Intraseasonal meridional current variability in the eastern equatorial Indian Ocean, *J. Geophys. Res.*, *109*, C07037, doi:10.1029/2007JC004331.
O'Neill, K. (1984), Equatorial velocity profiles: Part I: Meridional component, *J. Phys. Oceanogr.*, *14*, 1829–1841.
Proehl, J. A. (1990), Equatorial wave-mean flow interaction: The long Rossby waves, *J. Phys. Oceanogr.*, *260*, 274–294.
Sengupta, D., R. Senan, and B. N. Goswami (2001), Origin of intraseasonal variability of circulation in the tropical Indian Ocean, *Geophys. Res. Lett.*, *28*, 1267–1270.
Sengupta, D., R. Senan, V. S. N. Murty, and V. Fernando (2004), A biweekly mode in the equatorial Indian Ocean, *J. Geophys. Res.*, *109*, C10003, doi:10.1029/2004JC002329.
Shinoda, T. (2010), Observed dispersion relation of Yanai waves and 17-day tropical instability waves in the Pacific Ocean, *SOLA*, *6*, 17–20, doi:10.2151/sola.2010-005.
Shinoda, T. (2012), Observation of first and second baroclinic mode Yanai waves in the ocean, *Q. J. R. Meterol. Soc.*, *138*, 1018–1024, doi: 10.1002/qj.968.
Smith, T. A., S. Chen, T. Campbell, P. Martin, W. E. Rogers, S. Gabersek, D. Wang, S. Carroll, and R. Allard (2013), Oceanwave coupled modeling in coamps-tc: A study of hurricane Ivan (2004), *Ocean Modell.*, *69*, 181–194.
Soares, S. M., K. J. Richards, and A. Natarov (2014), Near inertial waves in the tropical Indian Ocean: Energy fluxes and dissipation, poster presented at Ocean Sciences Meeting, AGU, Honolulu.
Weisberg, R. H., A. Horigan, and C. Colin (1979), Equatorially trapped Rossby-gravity wave propagation in the Gulf of Guinea, *J. Phys. Oceanogr.*, *37*, 67–86.
Wheeler, M., and G. Kiladis (1999), Convectively coupled equatorial waves: Analysis of clouds and temperature in the wavenumber frequency domain, *J. Atmos. Sci.*, *56*, 374–399.
Wyrtki, K. (1973), An equatorial jet in the Indian Ocean, *Science*, *181*, 262–264.
Yanai, M., and T. Murayama (1966), Stratospheric wave disturbances propagating over the equatorial Pacific, *J. Meteorol. Soc. Jpn.*, *44*, 291–294.